Soft Matter

PAPER

View Article Online
View Journal | View Issue

Cite this: *Soft Matter*, 2026, **22**, 1863

Complex molecular dynamics of symmetric model discotic liquid crystals: comparison of hexakis(hepta-alkanoyloxy)triphenylene (HOT6) with hexakis(hexa-alkyloxy)triphenylene (HAT6)

Christina Krause,[a] Paulina Szymoniak,[a] Wiebke Lohstroh,[b] Fanni Juranyi,[c] Michaela Zamponi,[d] Bernhard Frick,[e] Dominik Al-Sabbagh,[a] Franziska Emmerling,[af] Reiner Zorn[g] and Andreas Schönhals *[ah]

This study investigates the complex molecular dynamics of discotic liquid crystals (DLCs) by comparing two structurally similar compounds: hexakis(hepta-alkanoyloxy)triphenylene (HOT6) and hexakis(hexa-alkyloxy)-triphenylene (HAT6) having the same triphenyl core and the same length of the alkyl side chain. The difference of both materials is that the alkyl chain is linked by an oxygen bridge to the triphenylene core for HAT6 and by a ester group for HOT6. Using a combination of broadband dielectric spectroscopy, differential scanning calorimetry, X-ray scattering, and neutron scattering techniques, the research explores the glass transition phenomena and relaxation processes in these materials. HOT6, featuring ester linkages, exhibits distinct dynamic behavior compared to HAT6, including two separate glass transitions indicated by the α_1- and α_2-relaxation found by dielectric spectroscopy which are assigned to the glassy dynamics of the alkyl side chain in the intercolumnar space and that of the columns, respectively. The study reveals that the ester group in HOT6 leads to increased molecular rigidity and altered packing in the intercolumnar space, as evidenced by X-ray scattering and the vibrational density of states. Neutron scattering confirms localized methyl group rotations and a further relaxation process which relates to the γ-relaxation revealed by dielectric spectroscopy. The findings contribute to a deeper understanding of glassy dynamics in partially ordered systems and highlight the influence of molecular architecture on relaxation behavior in DLCs.

Received 16th December 2025,
Accepted 5th February 2026

DOI: 10.1039/d5sm01247c

rsc.li/soft-matter-journal

Introduction

The molecular dynamics associated with the glass transition represent a central and unresolved issue in condensed matter physics (see for instance ref. 1–9). Despite extensive research, the fundamental mechanisms underlying the transition of a glass-forming system into a disordered, amorphous state – rather than crystallizing – remain only partially understood. A particularly challenging aspect is the pronounced increase in both the structural relaxation time, τ, and the viscosity as the system is cooled toward the thermal glass transition temperature, T_g.

Upon reducing the temperature by approximately a factor of two while approaching T_g, the relaxation time τ increases by more than 14 orders of magnitude. This dramatic change bridges microscopic and macroscopic time scales, highlighting the complexity of the underlying molecular processes. This phenomenon is referred to as α-relaxation (structural relaxation) or the dynamic glass transition.

At temperatures near T_g, the temperature dependence of the relaxation time τ, or equivalently the relaxation rate $f_p = 2\pi/\tau$, can be empirically described by the Vogel–Fulcher–Tammann (VFT) equation,[10–12] which reads

$$\ln f_p = \ln f_\infty - \frac{B}{T - T_0} \quad (1)$$

Here, f_∞ denotes the relaxation rate in the high-temperature limit, while B is a constant related to the fragility of the system.

[a] *Bundesanstalt für Materialforschung und -prüfung (BAM), Department Materials Chemistry, Unter den Eichen 87, 12205 Berlin, Germany. E-mail: Andreas.Schoenhals@bam.de; Fax: +49 30/8104-73384; Tel: +49 30/8104-3384*
[b] *Heinz Maier-Leibnitz Zentrum (MLZ), Technische Universität München, Lichtenbergstraße 1, 85748 Garching, Germany*
[c] *PSI Center for Neutron and Muon Sciences, 5232 Villigen PSI, Switzerland*
[d] *Forschungszentrum Jülich GmbH, Jülich Centre for Neutron Science at MLZ, Lichtenbergstr. 1, 85748 Garching, Germany*
[e] *Institut Laue-Langevin, 71 avenue des Martyrs, 38042 Grenoble Cedex 9, France*
[f] *Institut für Chemie, Humboldt Universität zu Berlin, Brook-Taylor-Straße 2, 12489 Berlin, Germany*
[g] *Forschungszentrum Jülich GmbH, Jülich Centre for Neutron Science (JCNS-1), 52425 Jülich, Germany*
[h] *Institut für Chemie, Technische Universität Berlin, Straße des 17. Juni 135, 10623 Berlin, Germany*

The concept of fragility in the context of the glass transition provides a valuable framework for categorizing glass-forming systems.[13,14] Systems are referred to as fragile when $f_p(T)$ exhibits a pronounced deviation from Arrhenius behavior, indicating a super-Arrhenius temperature dependence. In contrast, strong glass formers display a relaxation time that closely follows an Arrhenius-type temperature dependence. The fragility is characterized by the fragility strength parameter $D = B/T_0$. The temperature T_0, often termed the Vogel temperature or the ideal glass transition temperature, is derived from empirical fits using the VFT equation to $f_p(T)$. It typically lies 30–70 K below T_g as determined by conventional techniques such as differential scanning calorimetry (DSC). It is worth noting that it is known for a longer time that a transition from the VFT to an Arrhenius-like behavior has been observed above a temperature $T_B \approx 1.2...1.3T_g$ (see for instance[15,16]).

In the cooperativity-based approaches to the glass transition, which have been extensively discussed in the literature (see for instance ref. 17–20), the pronounced increase in relaxation time near the glass transition temperature is attributed to the notion that molecular rearrangements occur in a cooperative manner. Specifically, the movement of a given molecule requires the simultaneous reorganization of neighboring molecules within a complex and rugged energy landscape to reach a local or global energy minimum.

In addition to the primary α-relaxation process, further dynamical processes relevant to the glass transition have been identified. Notably, Goldstein and Johari introduced the concept of a so-called slow β-relaxation, which is considered a precursor to the α-relaxation, particularly in cases where the observed secondary relaxation cannot be attributed to internal molecular degrees of freedom (*i.e.*, a genuine β-relaxation). The temperature dependence of the β-relaxation rates typically follows an Arrhenius behavior, indicating a truly thermally activated process. The Arrhenius equation reads

$$f_p = f_\infty \exp\left(-\frac{E_A}{k_B T}\right). \quad (2)$$

Here E_A denotes the activation energy which is found in the range of 20 to 40 kJ mol^{-1}. k_B is the Boltzmann constant.

Besides relaxation processes, it is known that glasses show characteristic excess contributions to the low frequency vibrational density $g(\omega)$ (VDOS) of states compared with the prediction of the Debye theory which gives $g(\omega) \sim \omega^2$ based on the propagation of sound waves. In the reduced representation depicting $g(\omega)/\omega^2$ *versus* the angular frequency ω a peak is observed in the frequency range of 1.5 to 7.5 ps^{-1} (1 to 5 meV) which is referred to as the Boson peak.[21] Despite the Boson peak manifesting on picosecond timescales, its potential relevance to the glass transition – characterized by relaxation processes occurring on timescales of approximately 100 seconds or longer – remains a topic of active scientific debate.[22,23] The molecular origin of the Boson peak remains contentious. Theoretical models are commonly grouped into three categories. Within the soft potential model, the Boson peak is attributed to quasi-localized vibrations of atomic groups in soft potentials arising from structural disorder in amorphous systems which differ principally from sound waves (see for instance ref. 24–26). A second class of models interprets the Boson peak as a broadened and shifted analogue of the Van Hove singularity, assuming an underlying crystalline reference structure, with disorder-induced broadening and frequency shifts.[27] Notably, ref. 28 suggests that coupling between optical and acoustic modes may produce a pseudo Van Hove singularity. A third approach, proposed by Schirmacher *et al.*, combines elements of both previous discussed models, attributing the Boson peak to harmonic vibrations in a disordered elastic medium.[29] While retaining sound-wave characteristics and incorporating 'soft spots' akin to the soft potential model, it does not treat the Boson peak as a modified Van Hove singularity. Recently, a unified theoretical approach considering both Van Hove singularity and the Boson peak has been presented where the propagation and damping of phones is discussed as a mechanism.[30,31]

As discussed above, the cooperative dynamics underlying the glass transition were initially theorized by Adam and Gibbs, who introduced the concept of cooperatively rearranging regions (CRRs) to describe structural rearrangements within supercooled liquids.[17] Wynne *et al.* proposed that the Boson peak originates from molecular clusters consisting of approximately 20 molecules, which may correspond to cooperatively rearranging regions implicated in the dynamics of the glass transition.[32] Further evidence supporting this interpretation has been obtained through molecular dynamics simulations conducted on systems composed of symmetric molecules.[33]

The most extensively studied systems exhibiting glass transitions include low-molecular-weight liquids, silica-based glasses, and polymers. In addition to these well-known materials classes, glass transition phenomena can also occur in materials characterized by partial structural order and restricted molecular mobility.[13,14] Seki *et al.* were the first to report the occurrence of a glass transition in plastic crystals by calorimetry.[34] Additional examples of glass transitions in plastic crystalline systems are discussed in the literature (see for instance[35–39]). It is noteworthy that discotic liquid crystals also exhibit glass-like dynamic behavior, as discussed in previous studies.[40–50] To date, the molecular mechanisms underlying glassy dynamics in systems characterized by restricted mobility and partial order remain unresolved. Studies on such systems, including liquid crystals, may provide valuable insights into the general phenomena associated with the glass transition.

Discotic liquid crystals (DLCs) represent a class of advanced soft matter materials with significant potential for instance for applications in electronic devices (see for instance ref. 51–53 and references cited therein). DLCs are typically composed of molecules having a rigid, disc-shaped aromatic core or a self-assembled disc-like structure with flexible alkyl chains attached to the periphery. At low temperatures, DLCs often exhibit a plastic crystalline phase, which transitions upon heating to a hexagonal columnar liquid crystalline phase. In this phase, the discotic molecules stack into columns that behave as one-dimensional fluids,[54] with the columns themselves arranged on

a two-dimensional hexagonal lattice. The alkyl side chains fill the intercolumnar space. The unique properties and potential applications of DLCs are primarily associated with this hexagonally ordered liquid crystalline phase. In addition to the hexagonal columnar phase, nematic phases *etc.* can also be observed in certain DLC systems. Upon further temperature increase beyond the stability range of the columnar phase, DLCs undergo an isotropization transition, resulting in a disordered, isotropic liquid state.

Recently the molecular mobility of a triphenyl-based discotic liquid crystal, hexakis(hexa-alkyloxy)triphenylene (HAT6) was investigated by a combination of broadband dielectric spectroscopy, advanced dynamical calorimetry and quasielastic neutron scattering.[44] Here a comparable triphenyl-based DCL with an equal length of the alkyl side chains, hexexakis(hepta-alkanoyloxy)triphenylene (HOT6) was studied. Interest in the hexexakis(*n*-alkanoyloxy)triphenylenes comes from the additional fact that they are photoconductive and doped with few mol of an oxidant they become semiconductive.[55] The obtained results for HOT6 will be compared in detail with that of HAT6.

Materials und methods

Materials

Hexakis(hepta-alkanoyloxy)triphenylene (HOT6) was obtained from Synthon Chemicals (Bitterfeld, Germany). Its chemical structure is given in Fig. 1a in comparison with that of Hexakis(hexa-alkyloxy)triphenylene (HAT6) (see Fig. 1b). Both materials possess alkyl side chains of identical length, defined by the number of carbon atoms in the chain. The difference in the chemical structure of both materials is that the alkyl side chains are linked *via* an ester group to the triphenylene core for HOT6 while for HAT6 the alkyl side is connected to the core by an oxygen bridge. The ester group in HOT6 will dynamically decouple the alkyl side chain more from the triphenylene core than the oxygen bridge in HAT6. Moreover, as the ester linkage in HOT6 is bulkier than the oxygen group in HAT6, the HOT6 molecule is expected to be larger than the HAT6 one. It is worth noting that due to the presence of an ester group, HOT6 exhibits increased susceptibility to hydrolytic degradation under humid conditions compared with HAT6. HOT6 was used without further purification. The purity given by the producer is 94%. Fig. 1c presents a schematic of the self-assembly of the disc-like molecules to the columnar hexagonal liquid crystalline phase.

Methods

Differential scanning calorimetry (DSC). Conventional DSC measurements were carried out using a Seiko DSC 7020. The sample (mass ~ 10 mg) was measured from 173 K to 283 K with a heating and cooling rate of 10 K min^{-1}. Nitrogen was used as a protection gas at a flow rate of 20 ml min^{-1}. The second heating/cooling run is used for analysis. For background correction an empty pan was measured under the same condition as for the sample. The data measured for the empty pan was subtracted from that of the sample. Indium was used for calibration.

Fast scanning calorimetry (FSC). To investigate the molecular dynamics further FSC is used employing a Mettler-Toledo Flash DSC1. The Flash DSC1 is a chip-base power compensated DSC. The measurement cell is the twin chip sensor MultiSTAR UFS 1.[56] Due to the chip-based sensor architecture of the instrument, and the low sample masses heating rates ranging from 10 K s^{-1} up to 10 000 K s^{-1} can be achieved. Nitrogen was employed as the purge gas at a constant flow rate of 40 mL min^{-1}. The base temperature control was ensured using a Huber TC100 intercooler. Calibration of the Flash DSC 1 was performed in accordance with the specification of the manufacturer. This means that each calorimetric chip was calibrated by the producer. During the measurement the calibration data

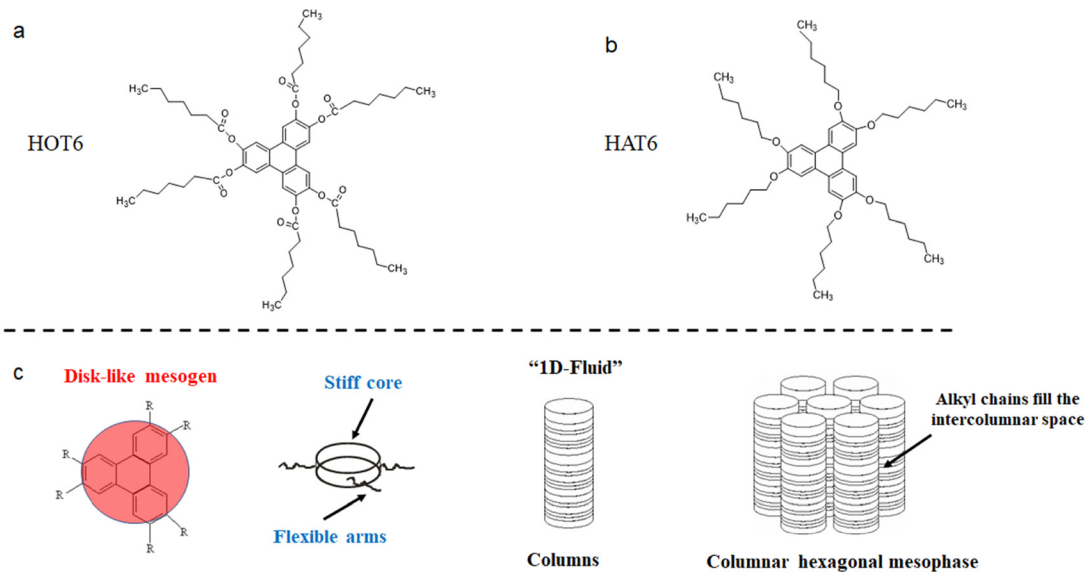

Fig. 1 Chemical structure of HOT6 (a) and HAT6 (b). (c) Schematics of the self-assembly of the discotic liquid crystal.

were automatically downloaded from the database of the producer.[56] The calibration was checked by measurements on standards leading to a maximal error in temperature of ±5 K in the whole considered temperature range. Thermal lag effects are minimized by considering low samples masses in the nanogram range and a thin film sample geometry. The typical error due to thermal lag under these conditions is smaller than the overall uncertainty in temperature. During the FSC experiment the heating rate was varied. To ensure the same history of the sample before each heating run the sample was cooled from the isotropic state to 193 K with a cooling rate of 1000 K s^{-1}.

X-ray scattering. The measurements were conducted at the synchrotron microfocus beamline μSpot, located at BESSY II (Helmholtz-Zentrum Berlin für Materialien und Energie). The optical configuration of the beam line, characterized by a divergence of less than 1 mrad in both horizontal and vertical directions, enables a focused beam diameter of 100 μm. Under standard operating conditions with a ring current of 100 mA, the photon flux reaches approximately 1×10^9 photons s^{-1}. All experiments were performed using monochromatic X-rays with a wavelength of 1.03358 Å, selected *via* a double-crystal monochromator employing Si(111) crystals.

Scattered X-ray intensities were recorded 820 mm downstream from the sample position using a two-dimensional X-ray detector (MarMosaic, CCD, 3072 × 3072 pixels), featuring a point spread function with an approximate width of 100 μm. A comprehensive description of the beamline setup can be found in ref. 57. The acquired scattering patterns were processed and transformed into intensity profiles as a function of the scattering vector q, where $q = (4\pi/\lambda_x)\sin\theta$ with θ being half the scattering angle 2θ, and λ_x the wavelength of the X-rays. Data reduction and analysis were performed using the software package FIT2D.[58]

For the X-ray scattering experiments, the samples were loaded into borosilicate glass capillaries (WJM-Glas Glastechnik & Konstruktion, Germany) with an outer diameter of 0.3 mm. To ensure consistency with the DSC measurements, the samples were heated at a controlled rate of 10 K min^{-1} during the experiments.

Dielectric spectroscopy. The complex dielectric function $\varepsilon^*(f) = \varepsilon'(f) - i\varepsilon''(f)$ is measured in the frequency range from 10^{-1} Hz to 10^6 Hz where ε' and ε'' represent the real (storage) and imaginary (loss) components of the complex dielectric function and f the frequency. All measurements were carried out in parallel plate capacitor geometry employing gold-plated brass electrodes. To ensure a consistent sample thickness of 50 μm, fused silica spacers were used. The diameter of the sample was 20 mm. The measurements were performed by a high-resolution Alpha analyzer interfaced to an active sample head (Novocontrol, Montabaur, Germany). For extended details see ref. 59. Temperature control of the sample was achieved by a Quatro temperature controller (Novocontrol) with a temperature stability better than 0.1 K.

Neutron scattering. Inelastic and quasielastic neutron scattering are sensitive to molecular motions at microscopic length and time scales.[60] During the scattering process, both momentum and energy are exchanged between the incident neutrons and the nuclei within the sample besides elastic scattering. The quantity that describes this interaction is the double differential scattering cross section, which characterizes the probability of neutrons being scattered into a specific solid angle Ω with a given measured energy transfer ΔE. The double differential scattering cross section is given by

$$\frac{d^2\sigma}{d\Omega d\omega} = \frac{1}{4\pi}\frac{k_f}{k_i}(\sigma_{coh}S_{coh}(q,\omega) + \sigma_{inc}S_{inc}(q,\omega)). \quad (3)$$

$\mathbf{k_i}$ and $\mathbf{k_f}$ are the incident and final wave vectors of the neutron beam respectively. The difference defines the scattering vector $\mathbf{q} = \mathbf{k_f} - \mathbf{k_i}$. The moduli of $\mathbf{k_i}$ and $\mathbf{k_f}$ are denoted as k_i and k_f in eqn (3). The modulus of $\mathbf{q}$ is referred to as q in the following. The angular frequency ω is directly related to ΔE *via* the expression $\Delta E = \hbar\omega$, where $\hbar$ denotes the reduced Planck constant. The functions $S_{inc}(q,\omega)$ and $S_{coh}(q,\omega)$ represent the incoherent and coherent dynamic structure factors, respectively, which describe the frequency and momentum dependent scattering behavior of the system. The parameters σ_{inc} and σ_{coh} denote the corresponding incoherent and coherent scattering cross-sections. The molecular composition of HOT6 comprises hydrogen (H), carbon (C), and oxygen (O) atoms. The corresponding macroscopic scattering cross-sections were calculated to $\Sigma_{coh} = 0.0334$ mm^{-1} and $\Sigma_{inc} = 0.4233$ mm^{-1}. Details of the calculations are given in the SI. The data indicate that the scattering is predominantly incoherent, which is due to the high incoherent scattering cross-section of hydrogen. It is noteworthy that most of the hydrogen nuclei are located within the alkyl side chains, which occupy the intercolumnar regions. Consequently, neutron scattering probes vibrations and molecular fluctuations in the intercolumnar space.

For the neutron scattering investigations different methods are combined:

Inelastic neutron scattering. For the measurement of the low frequency density of states inelastic neutron scattering is employed using the time-of-flight neutron scattering spectrometer TOFTOF.[61] TOFTOF is operated by Technische Universität München at the Heinz Maier-Leibnitz Zentrum (MLZ, Garching, Germany). All measurements were conducted using a standard configuration of TOFTOF. An incident neutron wavelength of λ_n = 5.6 Å was employed, yielding an instrumental energy resolution in the range of 55 to 63 μeV (full width at half maximum, FWHM), with resolution is increasing as a function of the scattering angle. In this configuration, the maximum accessible elastic momentum transfer is $q = 2.0$ $Å^{-1}$. The instrumental resolution $R(q,\Delta E)$ was determined by measuring the sample at $T = 4$ K, a temperature at which all molecular motions – except for quantum-mechanical zero-point vibrations – are expected to be frozen. To minimize the overlap of quasielastic contributions with inelastic scattering, the vibrational density of states (VDOS) was measured at $T = 80$ K. Data acquired from the TOFTOF spectrometer were analyzed using the INX software package, which includes modules for time-of-flight to energy conversion, background subtraction, vanadium standard normalization, and correction for self-attenuation effects.[62] An example for inelastic neutron scattering

raw data measured at TOFTOF is given in the SI (Fig. S1). $S_{inc}(q,\Delta E)$ displays characteristic excess vibrational contributions compared with the resolution of the spectrometer. The corresponding data for HAT6 were taken from an earlier experiment[82] on IN6 at Institut Laue-Langevin, Grenoble, France. Experimental details and the specifications of IN6 can be found in ref. 82.

Elastic scans. To investigate molecular dynamics on a timescale corresponding approximately to the resolution of a neutron backscattering spectrometer (*ca.* 2 ns), elastic fixed window scans ($\Delta E \approx 0$) were performed at the IN16 instrument, a neutron backscattering spectrometer of the second generation which was located at the Institut Laue-Langevin (ILL, Grenoble, France).[63] The neutron backscattering spectrometer IN16 was employed using unpolished Si(111) monochromators and analyzers, operating at a neutron wavelength of $\lambda = 6.271$ Å. The instrument provided an energy resolution of approximately 0.9 μeV and allowed access to momentum transfers up to a maximum of $q \approx 1.9$ Å^{-1}. The Doppler drive was set at rest ($\Delta E \approx 0$). Elastic scattering measurements at the lowest temperature were conducted with improved statistical precision, as this dataset serves as the reference point for subsequent analysis. The employed heating rate was 0.56 K min^{-1}. The raw data can be found elsewhere.[64]

An effective mean squared displacement, $\langle u^2\rangle_{eff}$, is derived from the measured elastic scattering intensity, $I_{el}(q)$, by fitting the function[65]

$$\frac{I_{el}(q)}{I_0(q)} = \exp\left(-\frac{\langle u^2\rangle_{eff} q^2/3}{1+\alpha_2\langle u^2\rangle_{eff} q^2/6}\right) \quad (4)$$

complemented by a multiple scattering term to the data. Here, $I_0(q)$ denotes the total scattered intensity measured at the lowest accessible temperature. In eqn (4), α_2 represents an effective non-Gaussian parameter introduced to account for deviations of the experimental data from the standard Gaussian model. The incorporation of multiple scattering effects into eqn (4) is given in detail in the SI of ref. 65. Compared with the conventional Gaussian model, this function provides higher reliability, particularly when the effective mean-squared displacement $\langle u^2\rangle_{eff}$ becomes large. Furthermore, no specific microscopic model is assumed, in contrast to the approach described in ref. 66. Up to fourth order in q, the expression is mathematically equivalent to a cumulant expansion incorporating a non-Gaussian parameter, α_2. However, unlike a truncated expansion at the q^4 term, this formulation avoids the unphysical increase of I_{el}/I_0 beyond unity. Moreover, eqn (4) is further supported by the theoretical framework of Singwi *et al.*, which describes the intermediate scattering function.[66] To have a compatibility with the result obtained for HOT6 here, the mean-squared displacement of HAT6 given in ref. 44 was recalculated using eqn (4). The percentage of multiple scattering events were 22.1% for HAT6 and 12.3% for HOT6. A comparison with the mean square displacement obtained in ref. 44 employing a fractal model[67] and $\langle u^2\rangle_{eff}(T)$ calculated by eqn (4) is given in the SI, Fig. S6.

Quasielastic neutron scattering (QENS). To extend the accessible time window in neutron scattering experiments, time-of-flight (TOF) spectroscopy was combined with neutron backscattering (BS) techniques. The TOF measurements were conducted on the spectrometer TOFTOF under the same configuration as described above. Data reduction was carried out with the software INX as given above.[62] An example of the TOF QENS measurement is given in the SI, Fig. S2. The spectra measured for higher temperatures show the characteristic quasielastic broadening compared with the resolution of TOFTOF.

Neutron backscattering spectra were taken at the high-resolution spectrometer SPHERES. SPHERES is a third-generation cold neutron backscattering spectrometer equipped with focusing optics and a rotating phase-space transform chopper. It is operated at the Heinz Maier-Leibnitz Zentrum by the Jülich Centre Neutron Science (JCNS), Forschungszentrum Jülich GmbH.[68,69] Measurements were conducted in the standard configuration, utilizing unpolished Si(111) monochromators and analyzers. The incident neutron wavelength was 6.271 Å, corresponding to an energy resolution of 0.65 μeV (full width at half maximum, FWHM) for the high-angle detectors. In this setup, the accessible momentum transfer range spans from 0.1 Å^{-1} to 1.8 Å^{-1}, but only data at and above 0.6 Å^{-1} were used for analysis because of the worse resolution and statistics for the small-angle detectors. The Doppler drive was set to achieve a maximal energy transfer of ±31 μeV. Like for TOFTOF the resolution of SPHERES $R(q,\Delta E)$ was obtained by measuring the sample at 4 K. Data obtained from the SPHERES spectrometer were processed using the SQW software,[70] which performs backscattering normalization, vanadium standard normalization, and corrections for self-attenuation. Additionally, the software applies an attenuation correction to the background prior to its subtraction. Fig. S3 presents the incoherent dynamic structure factor of HOT6 as measured with the SPHERES backscattering spectrometer at various temperatures. A temperature-dependent quasielastic broadening of the spectra relative to the instrumental resolution is observed, indicating an enhanced molecular mobility.

The analysis of the TOF and BS data by INX and SQW yield an effective dynamic structure factor, $S_{inc}(q,\Delta E)$, weighted by the respective scattering cross sections. Due to the significant difference in energy resolution between the TOFTOF and SPHERES spectrometers (see Fig. S2 and S3), the incoherent dynamic structure factors, $S_{inc}(q,\Delta E)$ were Fourier transformed and subsequently normalized by the Fourier transformation of the respective instrumental resolution functions. This procedure yields absolute values of the incoherent intermediate scattering function, $S_{inc}(q,t)$, enabling a consistent time-domain analysis of data acquired from both instruments. The $S_{inc}(q,t)$ datasets obtained from TOF and BS neutron spectroscopy were corrected for multiple scattering using a time-domain-based approach.[71] Due to the inability to precisely determine the scattering geometry, the multiple scattering contribution was treated as a fitting parameter and adjusted to satisfy the physical constraint $S_{inc}(q \to 0,t) = 1$. The optimized

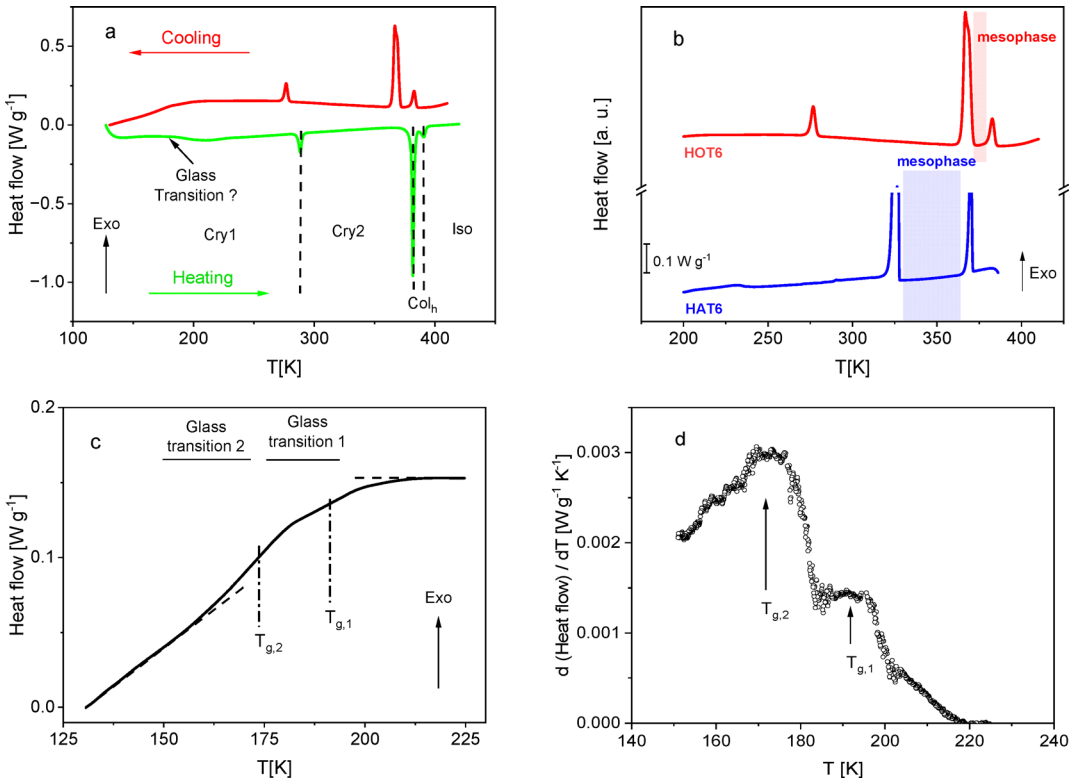

Fig. 2 (a) Heat flow *versus* temperature for HOT6. Blue – cooling, red – heating. Second cooling and heating. Rate 10 K min^{-1}. (b) Comparison of the heat flow for HOT6 (red) and HAT6 (blue). Data for HAT6 were taken from ref. 44. Second cooling, cooling rate 10 K min^{-1}. The heat flow for HOT6 was shifted along the *y*-scale for clarity. (c) Heat flow *versus* temperature for HOT6 at lower temperatures during cooling. (d) Derivative of the heat flow given in part c with respect to temperature. The arrows indicate the glass transition temperatures.

multiple scattering fractions were determined to be 31% (HAT6)/33% (HOT6) for SPHERES and 21% (HAT6)/22% (HOT6) for TOFTOF, relative to the single-scattering intensity.

Results and discussion

Differential scanning calorimetry and X-ray scattering

Fig. 2a gives the heat flow *versus* temperature for HOT6 for cooling and heating. At low temperature HOT6 has a plastic crystalline phase. At *ca.* 288 K (heating) HOT6 shows a crystal/crystal transition. This is different for HAT6 where such a crystal/crystal transition is not observed (see Fig. 2b). Most probably the observed crystal/crystal transition of HOT6 is due to the presence of the ester group which decouples the alkyl side chain dynamically more from the triphenyl core than the oxygen linkage in HAT6. At *ca.* 382 K HOT6 undergoes the transition from the plastic crystalline to the liquid crystalline Col$_h$ state followed by the phase transition to the "isotropic" state at *ca.* 391 K. The assignment of the phases corresponds to that given in the literature.[72] The phase transition temperatures of HOT6 in cooling and heating are given in comparison with data from the literature in Table 1. As known for other DCL systems there is a hysteresis between heating and cooling. Moreover, the values for the phase transitions temperatures measured here agree with the data given by the producer[73] and approximately with results presented in the literature.[72] This agreement supports the assignment of the phases. Like for HAT6 it is assumed for HOT6 that in the crystalline phases the tripenylene cores are arranged in columns where the alkyl side chains fill intercolumnar space.

Fig. 2b compares the heat flow for the second cooling for HOT6 and HAT6. This comparison shows that the temperature range of the Col$_h$ mesophase for HOT6 is much smaller than that of HAT6. Probably, the more flexible ester group of HOT6 compared with the oxygen bridge in HAT6 is the reason for the smaller mesophase range. Besides, the narrower temperature range of the mesophase Fig. 2b shows further that the phase transition enthalpies of all phase transition of HOT6 are much smaller than that of HAT6. Again, the lower phase transition enthalpies are due to the presence of the ester groups which might lead to less stable phases at higher temperatures.

Besides the peaks in the heat flow of HOT6 associated with the phase transition, a step-like change in the heat flow is observed in the temperature range between 150 K and 225 K (see Fig. 2a). This step-like change may indicate a glass transition of HOT6. A more detailed inspection of the low-temperature heat flow reveals a double-step structure (see Fig. 2c), which may suggest the presence of two distinct glass transitions. This becomes clearer considering the derivative of the heat flow with respect to temperature where a step-like change in the heat flow results in a peak. Although the derivative data shows some

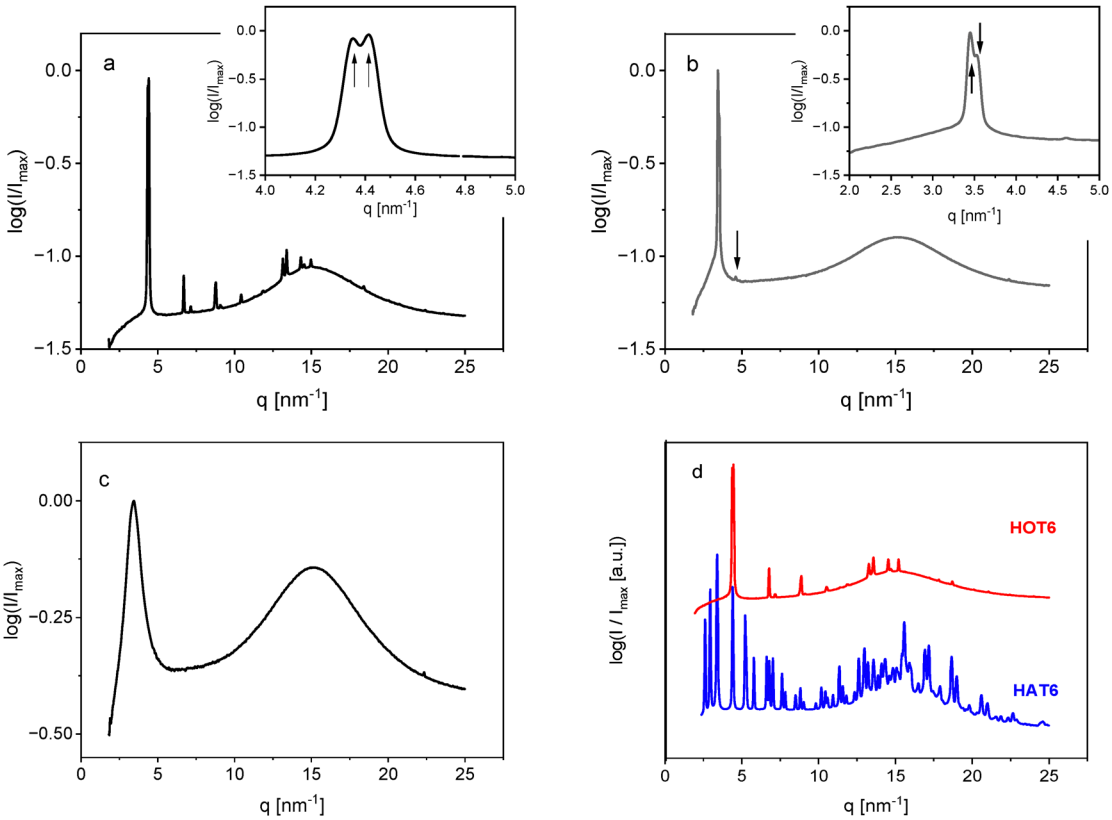

Fig. 3 (a) X-ray spectra of HOT6 in the Cry2 phase at T = 303 K. The inset enlarges the X-ray pattern in the q range from 4 nm^{-1} to 5 nm^{-1}. (b) X-Ray spectra of HOT6 in the Col$_h$ phase at T = 385 K. The inset enlarges the X-ray pattern in the q range from 2 nm^{-1} to 5 nm^{-1}. (c) X-ray spectra of HOT6 in the isotropic phase at T = 400 K. (d) Comparison of the X-ray pattern for HOT6 (red line) and HAT6 (blue line) at T = 303 K. The X-ray data for HOT6 are shifted by 1 for clarity.

Table 1 Phase transition temperatures of HOT6 in comparison to values given by the producer[73] and literature data[72]

	$T_{Cry1,Cry2}$ [K]	T_{Cry2,Col_h} [K]	$T_{Col_h,Iso}$ [K]
Cooling	277	367	383
Heating	288	382	390
Producer	—	379	381
Literature	—	342	366

scattering, Fig. 2d reveals two peaks which are well separated in temperature. From the maximum positions of the peaks the thermal glass transition temperatures are estimated. The glass transition observed at higher temperatures is denoted as glass transition 1 and that at lower temperatures as glass transition 2. It is worth noting that for HAT6 also two glass transitions are detected by calorimetric methods.[48] It is worth noting that the numeration of both glass transitions chosen here for HOT6 is analogues to that given for HAT6[48] for compatibility. The phenomenon will be discussed in more detail below.

Fig. 3 depicts the X-ray pattern for HOT6 in the different phases. In the Cry2 phase an X-ray pattern of a crystalline material with several sharp reflection peaks is observed (see Fig. 3a). Besides the sharp Bragg peaks in the q value range from *ca.* 10 nm^{-1} to 20 nm^{-1} an amorphous halo is observed which corresponds to average carbon–carbon correlations of the alkyl side chains.[74] In the columnar phase (see Fig. 3b), besides the amorphous halo the X-ray pattern, one relatively sharp reflection peak is visible. It corresponds to the average column–column distance d given by[75]

$$d = \frac{4\pi}{\sqrt{3}q_{max}} \quad (5)$$

From eqn (5) d = 2.1 nm is calculated for HOT6. Due to the presence of the bulkier ester group in HOT6 the intercolumnar distance is larger than for HAT6 (d = 1.8 nm) which features the smaller oxygen bridge.[83] Theoretically for a columnar phase higher order reflections at q values $\sim \sqrt{3}$ should be observed. These higher order reflections are not observed for HOT6. That might point to a less perfect columnar order in HOT6 Cry2 phase compared with that of HAT6 as it is already concluded from the phase transition enthalpies. However, an additional reflection is observed at a smaller q value than $\sqrt{3}q_{max}$ at *ca.* 4.6 nm.

A more detailed analysis of the X-ray diffraction pattern in the vicinity of the principal reflection peak for both the crystalline Cry2 and columnar phases reveals a distinct peak splitting into two subpeaks (see insets of Fig. 3a and b). This feature is absent in the corresponding patterns of HAT6. Given that the subpeaks occur at different q values for the crystalline and

columnar phases, the possibility of an experimental artifact can be reasonably excluded. The splitting of the peaks is discussed considering that the ester group can adopt different conformations. The specific conformations depend on several factors like the rotation around the single bond between the carbonyl carbon and the oxygen group/atom of the alkyl moiety, steric interactions with neighboring groups or molecules, intramolecular interactions, such as hydrogen bonding or π-interactions or crystal packing or supramolecular organization, which is particularly relevant in columnar phases. For simple esters, like present in HOT6, conformations are typically classified as *syn* or *anti*, depending on the relative orientation of the carbonyl group and the alkyl chain. These conformational differences can influence the effective length of the side chain, thereby affecting molecular packing and lattice parameters. These effects can lead to the observed peak splitting. However, to be visible as separate peak in the X-ray pattern there must be some clusters of a preferred conformation. The change of packing and lattice parameter are probably also the reason that higher order reflexes $\sim \sqrt{3}q_{max}$ are not observed. It might be further concluded that the different packing and lattice parameters results also in a different structure of the alkyl side chain in the intercolumnar space of HOT6 compared with HAT6.

In the isotropic state one broad Bragg peak is found (see Fig. 3c) which indicated a correlation of the triphenyl molecules also in this phase. The width of this reflection is much broader than that in the Col_h. This increased broadness of the peak which evidence a higher disorder in the "isotropic" state compared to Col_h phase. Also, the amorphous halo is found in the isotropic phase as expected.

Fig. 3d compares the X-ray pattern of HOT6 and HAT6 at T = 303 K. At this temperature HOT6 is the in the plastic crystal Cry2 state. Compared with HAT6 the X-ray scattering pattern that of HOT6 is less detailed. This points to a less ordered plastic crystalline structure in the Cry2 state compared with the plastic crystal state of HAT6. Unfortunately, no X-ray measurements could be carried out at temperatures where HOT6 is in the Cry1 phase which could be more comparable or even more ordered than the plastic crystal phase of HAT6.

Dielectric spectroscopy. Fig. 4a depicts the dielectric spectra of HOT6 as function of frequency and temperature in a 3D representation. In order of increasing temperature, a γ-relaxation is observed followed by a process which is called α_2-relaxation and a conductivity contribution. For compatibility the same notation of the relaxation processes is employed for HOT6 than for HAT6. At lower frequency characteristic for the α_2-relaxation a further relaxation process is detected which is called α_1-relaxation. For HAT6 a dielectric spectrum is observed which is comparable in some points (see Fig. 4b). Firstly, it is worth noting that the dielectric loss of HOT6 is higher than that of HAT6. This increased dielectric loss is due to the presence of the ester groups in HOT6 which have a higher dipole moment than the oxygen bridge in HAT6. Secondly, the α_1-relaxation is not detected in the dielectric spectra of HAT6 but it is observed by a combination of different calorimetric methods.[44] The result that the α_1-relaxation is found by dielectric spectroscopy for HOT6 is also attributed to the presence of the ester groups in that material.

The γ-relaxation of HOT6 is analyzed by standard methods fitting the model function of Havriliak/Negami (see SI, Section fitting of dielectric data by the HN-function) to the dielectric loss. For details see ref. 76. From the fits, the frequency of maximal loss f_p is obtained which is called relaxation rate. Fig. 5 depicts the temperature dependence of the of the logarithm of the relaxation rates of the γ-relaxation *versus* inverse temperature in the relaxation map or Arrhenius diagram. Fig. 5a gives the data for HOT6 and Fig. 5b for HAT6. $f_p(T)$ for the γ-relaxation is linear when plotted *versus* $1/T$ and can be therefore described by the Arrhenius equation. For HOT6 a value of the activation energy of 29.2 kJ mol^{-1} is obtained while for HAT6 a value of 20.6 kJ mol^{-1} is reported in ref. 44. The γ-relaxation of HAT6 and of other discotic liquid crystals is assigned to localized fluctuations of methylene units of the alkyl chains filling the intercolumnar space involving also polar groups.[42–50] Therefore, also the γ-relaxation of HOT6 is assigned to localized fluctuations of CH_2 units of the alkyl chains in the intercolumnar space. In ref. 48 the activation energy of the γ-relaxation for the series homologous of HATn (n = 5, 6, 8, 10, 12) with that of polyethylene. The value of the activation

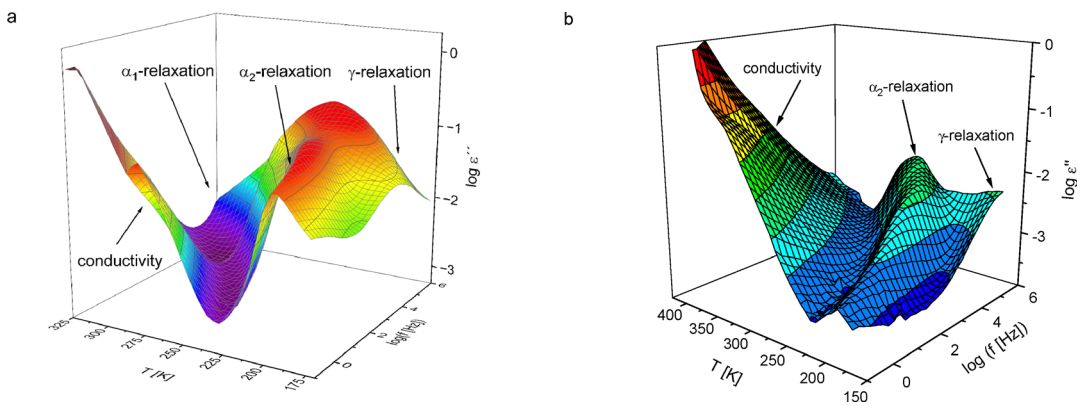

Fig. 4 Dielectric loss *versus* frequency and temperature in a 3D representation: (a) HOT6; (b) HAT6. The figure for HAT6 was adopted from ref. 44.

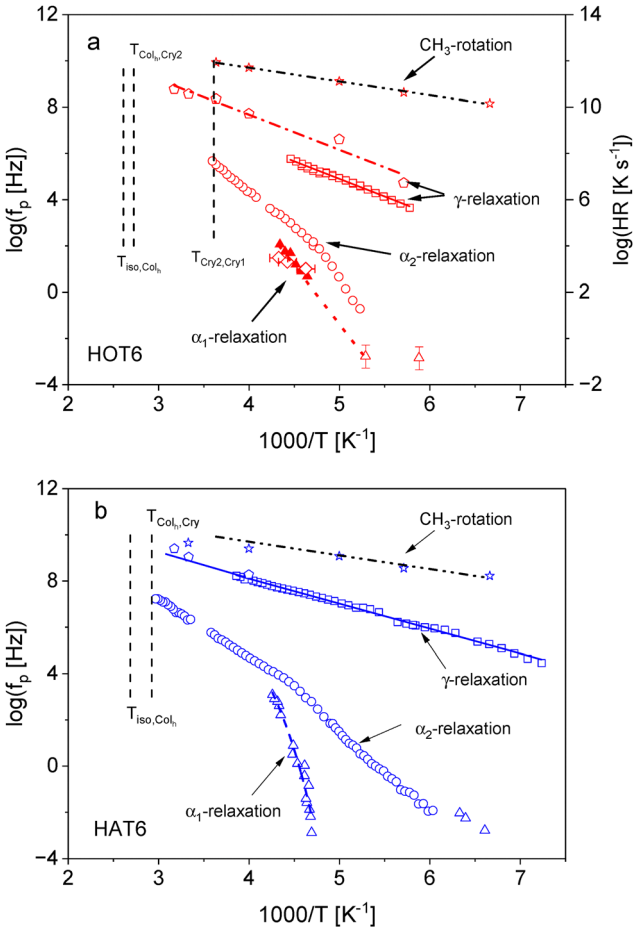

Fig. 5 (a) Relaxation map for HOT6 in Arrhenius coordinates: asterisks – methyl group rotation. The dashed dotted–dotted line is a common fit of the Arrhenius equation to the data of HOT6 and HAT6. Squares – dielectric γ-relaxation. The solid lines are fits of the Arrhenius equation to the corresponding data. Pentagons – second process measured by neutron scattering. The dashed dotted line is a fit of the Arrhenius equation to the relaxation rates of the second process measured by neutron scattering. The red dashed-dotted line is a fit of the Arrhenius equation to the data of HOT6. Circles – dielectric α_2-relaxation. Solid triangles – dielectric α_1-relaxation diamonds – heating rate (HR) *versus* inverse glass transition temperature estimated from the FSC measurements. Open triangles – HR *versus* inverse T_g taken from the DSC measurements. The dotted line is a linear fit to heating rates of FSC and $T_{g,1}$ measured by DSC. Phase transitions temperatures are indicated by black dotted lines. (b) Relaxation map for HAT6 in Arrhenius coordinates. All data were taken from ref. 48: asterisks – methyl group rotation. The dashed dotted–dotted line is a common fit of the Arrhenius equation to the data of HOT6 and HAT6. Squares – dielectric γ-relaxation. The solid lines are fits of the Arrhenius equation to the corresponding data. Pentagons – second process measured by neutron scattering. The solid blue line is a fit of the Arhenius equation to the data of the γ-relaxation. Triangles – thermal data for the α_1-relaxation. The dashed line is a fit of the VFT equation to the thermal data. Phase transitions temperatures are indicated by black dotted lines.

energy of the γ-relaxation estimated for HOT6 is closer to the activation energy of *ca.* 40 kJ mol^{-1} of the γ-relaxation of polyethylene (PE)[77] one must conclude that the molecular fluctuations responsible for the γ-relaxation of HOT6 are more restricted than that of HAT6. At the first glance that seems to disagree with the conclusion drawn from the X-ray measurements that the Cry2 phase is less ordered that the plastic crystalline state of HAT6. However, the γ-relaxation of HOT6 takes place at lower temperature in the Cry1 phase of HOT6. Although no X-ray data for the Cry1 phase are available it is concluded that the Cry1 state of HOT6 is more ordered than that of HAT6.

At low temperature the α_2-relaxation of HOT6 can be also analyzed by fitting the HN model function directly to the data. However, at higher temperatures the α_2-relaxation overlaps with the γ-relaxation which prevents a reliable analysis of the α_2-relaxation (see Fig. 4a). Therefore, that process is further analyzed by a so-called derivative approach.[78] It has been demonstrated that the Debye function exhibits the following behavior:

$$\varepsilon''_{\mathrm{Deriv}} = -\frac{\pi}{2}\frac{\mathrm{d}\varepsilon'}{\mathrm{d}\ln(\omega)} = \varepsilon''^{2} \tag{6}$$

Owing to the squared dependence in the derivative of the dielectric function, $\varepsilon''_{\mathrm{Deriv}}$, the width of the conduction-free loss peak is narrower than that of the primary dielectric loss function ε'' leading to a separation of overlapping relaxation processes. Details and examples for this analysis are given in the SI (Section Analysis of dielectric spectra by the derivative approach). Fig. 5 compares the temperature dependence of the relaxation rates of the α_2-relaxation of HOT6 (Fig. 5a) with that of HAT6 (Fig. 5b). The α_2-relaxation of HOT6 is observed in a comparable temperature/frequency window than that of HAT6. In ref. 44 evidence was presented that the α_2-relaxation is related to a glassy mobility of the columns, which can be considered as glassy dynamics of a one-dimensional liquid. As the core of HOT6 is analogous to that of HAT6 and because the α_2-relaxation for HOT6 is observed in a comparable temperature/frequency, the α_2-relaxation of HOT6 is also assigned to glassy mobility of the columns. Like for HAT6 the temperature dependence of the relaxation rates of the α_2-relaxation is quite complex and can be described neither by the Arrhenius nor by the VFT equation. Firstly, $f_p(T)$ increases relatively strongly with increasing temperature up to *ca.* 210 K following approximately the Arrhenius law. Secondly, at higher temperatures $f_p(T)$ increases further Arrhenius-like but with a lower apparent activation energy (see Fig. 5). For HAT6 the change in $f_p(T)$ correlates with the thermal glass transition temperature $T_{g,1}$ (see Fig. 5b). Although $T_{g,1}$ of HOT6 is found close to the change of $f_p(T)$, no exact correlation is found for HOT6. Nevertheless, it is argued that the change in the temperature dependence of the α_2-relaxation is related to the glass transition 2 which is assigned to the glass transition of the alkyl side chains in the intercolumnar space.

From the DSC measurements a thermal relaxation rate can be estimated by[79]

$$f_p = \frac{\dot{T}}{2\pi a \Delta T_g}. \tag{7}$$

The heating or cooling rate is denoted as $\dot{T}$ and ΔT_g is the width of the glass transition. ΔT_g is estimated as temperature

difference between onset and endset of the glass transition step a is a constant of the order of one. The thermal relaxation rate estimated for the glass transition 2 is added to the relaxation map (Fig. 5a). It correlates approximately with the lower temperature branch of the α_2-relaxation which supports the assignment of the α_2-relaxation to the glass-like mobility within the columns.

In addition to the well-established α_2-relaxation, the dielectric spectra of HOT6 reveal an additional an α_1-process, which is not detectable in the dielectric response of HAT6 (see Fig. 4) but has been identified through advanced calorimetric techniques. The α_1-relaxation in HOT6 was further analyzed using the derivative approach described previously (see SI). The corresponding relaxation rates were incorporated into the relaxation map (Fig. 5a). The dielectric α_1-process occurs in a comparable temperature/frequency window as the α_1-relaxation of HAT6 measured by a combination of calorimetric methods. In ref. 44 the α_1-relaxation was attributed to the glassy dynamics of the alkyl chains in the intercolumnar space. A similar interpretation is made here for the molecular origin of the α_1-relaxation of HOT6, supported by the correlation between dielectric and thermal relaxation rates derived from the glass transition 1 measured *via* DSC.

To investigate the glassy dynamics of HOT6 further fast scanning calorimetric measurements employing the Flash DSC1 have been carried out. An example for these measurements is given in the SI (Section Fast scanning calorimetry). From these measurements a thermal glass transition temperature is estimated by a derivative technique as described for the DSC measurements. As the data show considerable scatter, no thermal relaxation rates for FSC measurements according to eqn (7) can be extracted as the width ΔT_g cannot be estimated unambiguously. Therefore, the heating rates (HR) are plotted *versus* the inverse of the estimated glass transition temperature in Fig. 5a (right *y*-axis). The absolute values and the temperature dependence of the FSC data agrees with that of the dielectric α_1-relaxation of HOT6. Moreover, the heating rate and corresponding T_g estimated for the glass transition 1 measured by DSC were added to the heating rate plot. Both data sets agree with each other and can be described by a common fit of the Arrhenius equation. From these agreements it is concluded that the dielectric α_1-relaxation of HOT6 is really a glass transition.

While the temperature dependence of the relaxation rates of the α_1-process in HAT6 follows the VFT behavior, that of the α_1-relaxation of HOT6 seems to follow the Arrhenius equation. Within the framework of the fragility concept to the glass transition, this suggests that the α_1-relaxation in HOT6 exhibits stronger (*i.e.*, less fragile) glassy dynamics compared to that of HAT6. Consistent with conclusions drawn regarding the γ-relaxation, the Cry1 phase of HOT6 is structurally more ordered than the plastic crystalline phase of HAT6. This increased order likely imposes stronger constraints on the mobility of the alkyl side chains, resulting in more localized fluctuations of the alkyl chains relative to those of HAT6.

It is worth mentioning that glass transition 2 could not be investigated by FSC due to the limitations of Flash DSC1.

Neutron scattering

Inelastic neutron scattering – low frequency density of states. The determination of the low frequency vibrational density of states $g(\omega)$ from neutron scattering measurements is grounded in the conventional theoretical framework of one-phonon scattering under the incoherent approximation.[80] This approach presumes the presence of a single atomic species, thereby simplifying the analysis. Within this context, the VDOS is quantitatively linked to the incoherent dynamic structure factor by:

$$S_{\mathrm{inc}}(q,\omega) = \mathrm{e}^{-2W(q)}\left(\delta(\omega) + \frac{\hbar q^2}{2\bar{m}}\frac{g(\omega)}{\omega} \times \left(\exp\left(\frac{\hbar\omega}{k_{\mathrm{B}}T}\right) - 1\right)^{-1}\right) \tag{8a}$$

The exponential term $\mathrm{e}^{-2W(q)}$ is the Debye–Waller factor and δ represents the delta function. $\bar{m}$ gives the average atomic mass. Owing to the high incoherent scattering cross-section and the low atomic mass of hydrogen, its dynamical contributions are disproportionately amplified in the neutron scattering signal. Nevertheless, if the vibrational modes associated with hydrogen atoms are uniformly distributed across the relevant frequency range, the resulting spectral signal may be considered a valid representation of the VDOS from a thermodynamic perspective.

The experimentally observed scattering intensity, $S_{\mathrm{obs}}(q,\omega)$, corresponds to the convolution of the intrinsic scattering response of the sample with the instrumental resolution function of the spectrometer. Given that the Boson peak typically appears as a broad spectral feature, this convolution can be effectively approximated by a discrete summation. Under this approximation, eqn (8a) simplifies to:[81]

$$\begin{aligned} S_{\mathrm{obs}}(q,\omega) &= S_{\mathrm{inc}}(q,\omega) \otimes R(q,\omega) \\ &\approx \mathrm{e}^{-2W(q)}\left(R(q,\omega) + \frac{\hbar q^2}{2\bar{m}}\frac{g(\omega)}{\omega} \times \left(\exp\left(\frac{\hbar\omega}{k_{\mathrm{B}}T}\right) - 1\right)^{-1}\right) \end{aligned} \tag{8b}$$

$R(q,\omega)$ represents the resolution of the spectrometer. Eqn (8b) describes a linear relationship between $g(\omega)$ and $R(q,\omega)$. By acquiring scattering data at two distinct temperatures (in this case, 4 K and 80 K), it is possible to estimate both $g(\omega)$ and $R(\omega)$ from eqn (8b). The detailed procedure for the calculation of the VDOS is given in the SI. This calculation also includes a correction for multiple scattering events. At this point it must be mentioned that in earlier publication[78] this correction has not been made, leading to apparently higher values of $g(\omega)$. But due to the linear nature of the correction, this does not affect the shape and peak position of the result.

Fig. 6 compares $g(\omega)/\omega^2$ *versus* frequency for HOT6 and HAT6. As known from ref. 82 $g(\omega)/\omega^2$ *versus* ω shows a broad Boson peak for HAT6 with a maximum frequency ω_{BP} of *ca.* 2.77 ps^{-1}. This is a bit different for HOT6. Besides a main peak at a frequency of approximately 3.1 ps^{-1}, $g(\omega)/\omega^2$ *versus* frequency shows a broad shoulder in the frequency range of 4 ps^{-1} to 8 ps^{-1} which is not present for HAT6.

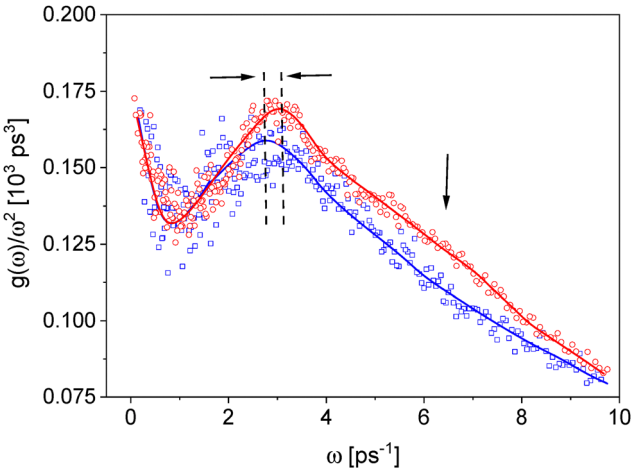

Fig. 6 Comparison of the low frequency vibrational density of states normalized by ω^2 *vs.* frequency for HOT6 (red spheres) and HAT6 (blue squares). Lines are guides to the eyes for the corresponding data. The lines are obtained by a smoothing approach. Dashed lines indicate the maximum positions of the BPs.

Firstly, the shift in the main maximum frequency position of HOT6 in comparison to that of HAT6 will be discussed. Within the framework of elastic disorder models addressing the Boson peak, the characteristic frequency of the BP is commonly associated with the elastic moduli of the material.[83] In materials with a reduced stiffness (softer materials) on a local scale, the Boson peak is observed to shift toward lower frequencies compared with stiffer (harder) counterparts. To validate this correlation, experimental studies have been conducted in which the mechanical stiffness of the material was systematically modulated – either through continuous structural modifications[82] or by incorporating an additional component into the host matrix.[84] Recently, this approach has been extended to investigate the correlation between the frequency position of the Boson peak and the Brunauer–Emmett–Teller (BET) surface area in intrinsic microporous polymers.[85–87] The higher value of ω_{BP} for HOT6 in comparison with that of HAT6 would imply that HOT6 is stiffer on a molecular scale in comparison to HAT6. This conclusion agrees with the results obtained by dielectric spectroscopy that the alkyl chains in the intercolumnar space are more constrained for HOT6 than that of HAT6 leading to a higher local elastic modulus.

Secondly, the shoulder in $g(\omega)/\omega^2$ *versus* ω observed in the frequency range of *ca.* 4 ps^{-1} to 8 ps^{-1} for HOT6 will be addressed (see Fig. 6). From the dielectric experiments, it was concluded that the structure of the alkyl side chains in the intercolumnar space is changed for HOT6 in comparison to that of HAT6. Most probably the changed packing and structure of the alkyl chains for HOT6 leads to additional vibrations giving rise to the shoulder in the VDOS of HOT6.

Elastic scans. Fixed elastic window scans are a powerful tool to monitor the molecular dynamics of a material at a time scale corresponding to the resolution of a neutron back scattering spectrometer.[88,89] Fig. 7a compares the effective mean squared displacement $\langle u^2\rangle_{eff}$ *versus* temperature for HAT6 and HOT6. As a first result, the phase transitions can be verified in the temperature dependence of $\langle u^2\rangle_{eff}$ for both materials. The inset of Fig. 7a enlarges the temperature scale of the effective mean squared displacement for HOT6 in the lower temperature range. Multiple processes can be identified from variations in the temperature dependence of the effective mean squared displacement. At low temperature the change of $\langle u^2\rangle_{eff}(T)$ is due to vibrations. This linear increase of $\langle u^2\rangle_{eff}$ with temperature is predicted theoretically.[80] At temperatures from 100 K to 150 K the temperature dependence of $\langle u^2\rangle_{eff}$ changes due to onset of the methyl group rotation as HOT6 like HAT6 has six methyl groups per molecule.[90] In the temperature range between 150 K and approximately 270 K, additional changes in the temperature dependence of the effective mean-square displacement, $\langle u^2\rangle_{eff}$ (T), are observed for HOT6. This behavior is attributed to the onset of the relaxation processes like the γ- and the α-relaxations, which are corroborated by dielectric spectroscopy measurements. The assignment of the methyl group rotation and the further relaxation process agree with the quasielastic neutron scattering discussed below. At *ca.* 300 K a

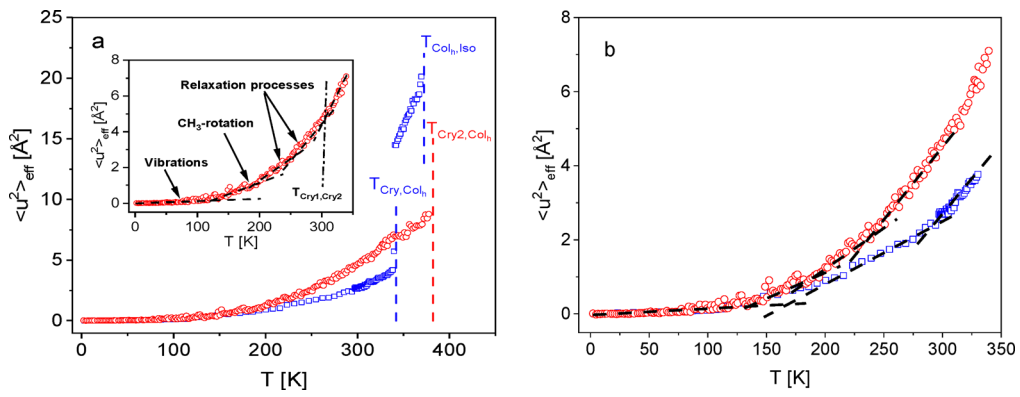

Fig. 7 (a) Temperature dependence of the effective mean squared displacement $\langle u^2\rangle_{eff}$: red circles – HOT6, blue squares – HAT6. The dashed lines represent the phase transition temperatures measured by DSC. The inset enlarges the temperature scale for HOT6 in the lower temperature range. The dashed lines are linear to the data in the corresponding temperatures ranges. (b) Comparison of $\langle u^2\rangle_{eff}$ (T) in the lower temperature range for HOT6 (red circles) and HAT6 (blue squares). The dashed lines are linear to the data in the corresponding temperatures ranges.

further change in $\langle u^2\rangle_{\mathrm{eff}}(T)$ is revealed for HOT6 which is attributed to the Cry1/Cry2 phase transition.

Fig. 7b compares the temperature dependence of $\langle u^2\rangle_{\mathrm{eff}}$ of HOT6 and HAT6 in the lower temperature range. In the temperature where the vibrations are revealed in the elastic scans the effective mean squared displacement for both materials are approximately similar as the vibrations are localized. As the methyl group rotation is also a localized relaxation process, the mean squared displacement is also approximately similar for this relaxation process. For temperatures above than characteristic for the methyl group rotation, $\langle u^2\rangle_{\mathrm{eff}}(T)$ is essential higher for HOT6 compared with that of HAT6. This behavior indicates that the molecular mobility in HOT6 is higher than for HAT6. Moreover, for HOT6 the temperature dependence of $\langle u^2\rangle_{\mathrm{eff}}$ seems to be more complex than that of HAT6.

Quasielastic neutron scattering. Fig. 8a depicts the incoherent intermediate (time dependent) scattering function $S_{\mathrm{Inc}}(q,t)$ for the used q values at 150 K. The data in the time range from 0.1 ps to *ca.* 30 ps were acquired using the TOFTOF spectrometer, whereas measurements for the range from *ca.* 60 ps to approximately 3 ns were conducted on the SPHERES instrument. At 150 K $S_{\mathrm{Inc}}(q,t)$ shows a single-step decay indicating a relaxation process which is assigned to the methyl group rotation. In general, the rotation rate distribution model is employed to analyze the methyl group rotation.[90] However, for simplicity here a stretched exponential is fitted to $S_{\mathrm{Inc}}(q,t)$. The fit function reads

$$S_{\mathrm{Inc}}(q,t) = \mathrm{DWF} \times \left((1-\mathrm{EISF_M})\exp\left(-\left(\frac{t}{\tau_{\mathrm{M}}}\right)^{\beta_{\mathrm{M}}}\right) + \mathrm{EISF_M}\right) \quad (9)$$

where DWF denotes the Debye–Waller factor, $\mathrm{EISF_M}$ symbolizes the elastic incoherent structure factor for methyl group rotation, τ_{M} is the relaxation time for methyl group rotation and β_{M} the corresponding stretching parameter. Fig. 8a shows that this approach describes the data well.

The q dependence of the $\mathrm{EISF_M}$ can be most effectively described by a model based on jump rotation within a threefold rotational potential. This potential is given by $V(\phi) \sim (1 - \cos(3\phi))/2$ which reflects the presence of three energetically equivalent minima corresponding to the rotational symmetry of the methyl group around its axis. This model captures the essential physics of the rotational dynamics and leads to an analytical expression for the $\mathrm{EISF_M}$[90,91]

$$\mathrm{EISF_M}(q) = \frac{1}{3}\left(1 + 2\frac{\sin(\sqrt{3}qr)}{\sqrt{3}qr}\right) \quad (10a)$$

The spatial arrangement of the hydrogen nuclei in a methyl group defines a circular trajectory with a radius of r = 1.027 Å. The theoretical prediction of eqn (10a) is given in Fig. 8b. During the deduction of eqn (10a) it was assumed that all hydrogen nuclei in a system undergo the methyl group rotation. Fig. 1a shows that is not true as HOT6 contains 84 hydrogen nuclei into total of which only 18 are in the methyl groups. Therefore eqn (10a) must be corrected by

$$\mathrm{EISF_{M,corr}}(q) = (1 - C_{\mathrm{fix}})\mathrm{EISF_M}(q) + C_{\mathrm{fix}} \quad (10b)$$

taking only into account the number of hydrogen nuclei which undergo the methyl group rotation. Here C_{fix} is the ratio $(n_{\mathrm{H,total}} - n_{\mathrm{H,methyl\,group}})/n_{\mathrm{H,total}}$ = 0.785. Fig. 8b reveals that this approach describes the data well. Fig. 8b shows further that the q dependence of the EISF for HOT6 is identical to that of HAT6 within error bars. This should be expected as the number of hydrogen nuclei in the methyl groups is identical for both materials, and the methyl group rotation is a localized process and thus independent of the linkage of the alkyl side chain to the triphenylene core.

From the relaxation time τ_{M} obtained by the fit of eqn (9) to the data a mean relaxation time can be calculated by

$$\langle\tau_{\mathrm{av}}\rangle = \frac{\tau}{\beta}\Gamma(\beta^{-1}). \quad (11)$$

In eqn (11) $\Gamma(x)$ denotes the Gamma function. The relaxation times for the methyl group rotation are independent of the q

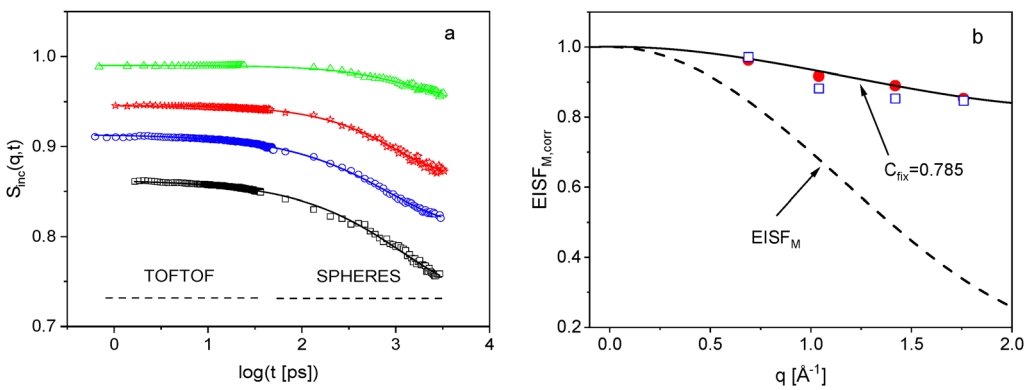

Fig. 8 (a) Incoherent intermediate scattering function $S_{\mathrm{Inc}}(q,t)$ of HOT6 *versus* time at T = 150 K at different values of the q vector: black squares q = 1.78 Å^{-1}; blue circles q = 1.42 Å^{-1}, red asterisk $-q$ = 1.04 Å^{-1} and green triangle $-q$ = 0.69 Å^{-1}. Lines are fits of eqn (9) to the data. (b) EISF *versus* q for HOT6 (solid red circles) and HAT6 (open blue squares). The dashed line is the prediction of eqn (10a). The solid line is calculated by eqn (10b) with C_{fix} = 0.785.

value which is expected for a localized relaxation process. Therefore, an arithmetically average relaxation time is calculated for each temperature. The relaxation rates for the methyl group of HOT6 are included in Fig. 5a and compared with those of HAT6. Both sets of data for the methyl group rotation can be described by a common Arrhenius equation with an average activation energy of approximately 11.3 kJ mol^{-1}. This is expected as the methyl group rotation is a localized relaxation process and should be independent from the linker of the alkyl side chain to the triphenyl core.

Fig. 9a compares the time dependence of $S_{inc}(q,t)$ for HOT6 and HAT6 for a q value of 1.79 Å^{-1} at T = 250 K. As already concluded from the elastic scans, for HOT6 the intermediate scattering function decays much stronger for HOT6 than for HAT6. As most of the scattering is due to the hydrogen nuclei located in the intercolumnar space, that indicates that the structure of the intercolumnar state is different for HOT6 compared to HAT6. Moreover, for temperatures higher than 150 K, $S_{inc}(q,t)$ exhibits a two-step decay. This indicates two underlying relaxation processes where the process at shorter times is methyl group rotation. To analyze the intermediate (time dependent) scattering function for these temperatures, two stretched exponentials are fitted to $S_{inc}(q,t)$ for temperatures higher than T = 150 K. The whole fit function reads

$$S_{Inc}(q,t) = \mathrm{DWF} \times \left((1 - \mathrm{EISF_M}) \exp\left(-\left(\frac{t}{\tau_M}\right)^{\beta_M} \right) + (\mathrm{EISF_M} - \mathrm{EISF}_\gamma) \exp\left(-\left(\frac{t}{\tau_\gamma}\right)^{\beta_\gamma} \right) + \mathrm{EISF}_\gamma \right). \quad (12)$$

EISF$_\gamma$, τ_γ and β_γ are the corresponding elastic incoherent structure factor, the relaxation time and the shape parameter for the relaxation process taking place observed at longer times. Examples for the fit of eqn (12) to the data are given in Fig. 9b. To reduce the number of free fit parameters it was assumed that the elastic incoherent structure factor is independent of temperature. This assumption is supported by the result that the q dependence follows eqn (10b) with a value of C_{fix} estimated from the chemical structure of HOT6. Therefore, the values of the EISF$_M$ obtained at T = 150 K were fixed for the fits of eqn (12) to the data measured at higher temperatures. Moreover, for β_γ the value obtained from the dielectric experiment was taken and fixed during the fits. The average relaxation for the process at longer times is calculated by eqn (11). As for the methyl group rotation, the relaxation times for the process observed at longer times are independent of the q vector within error bars which points to a localized relaxation process. The relaxation times were arithmetically averaged with respect to q. The corresponding relaxation rates are included in Fig. 5a.

For HAT6 the relaxation rates of the low frequency process observed with neutron scattering correspond in both its absolute values and its activation energy with that of the γ-relaxation found by dielectric spectroscopy (see Fig. 5b). This is a bit different for HOT6. Here the values of the relaxation rates observed by neutron scattering are by *ca.* 1 decade higher than that estimated by dielectric spectroscopy. However, the deduced activation energy of 29 kJ mol^{-1} for the relaxation process observed by neutron scattering is similar to that found for the γ-relaxation by dielectric spectroscopy (29.2 kJ mol^{-1}) (see Fig. 5a). Therefore, it is concluded that the relaxation process observed by neutron scattering is at least related to the dielectric γ-relaxation. It might be further argued that dielectric and neutron scattering sense different aspects of the same process.

Conclusion

This study presents a comprehensive comparison of the molecular dynamics of two structurally related discotic liquid crystals, HOT6 and HAT6, using a multi-technique approach including dielectric spectroscopy, calorimetry, X-ray scattering, and neutron scattering. The substitution of an oxygen bridge in HAT6 with an ester linkage in HOT6 significantly alters the dynamic behavior and structural organization of the material in the intercolumnar space. Also, the dielectric loss of HOT6 is enhanced compared to that of HAT6 which is due to the

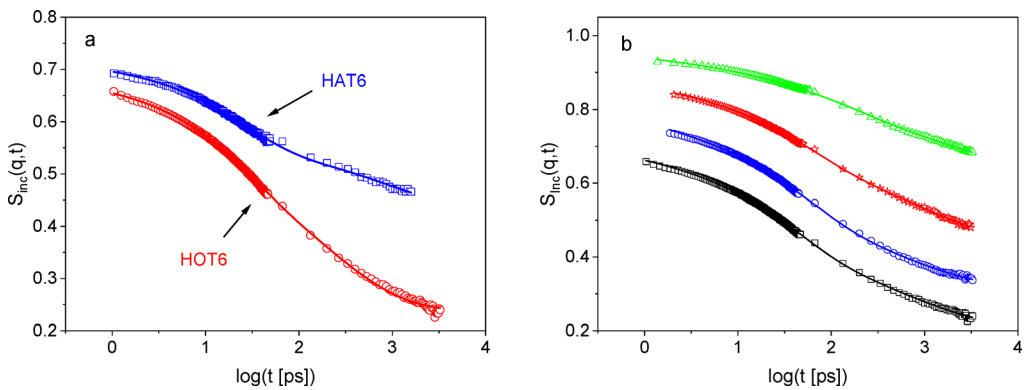

Fig. 9 (a) Comparison of the incoherent intermediated scattering function $S_{inc}(q,t)$ of HOT6 (red circles) and HAT6 (blue squares) for a q vector of 1.78 Å^{-1} at T = 250 K. Lines are guides to the eyes. (b) $S_{inc}(q,t)$ of HOT6 *versus* time at T = 250 K for different values of the q vector: black squares q = 1.78 Å^{-1}; blue circles q = 1.42 Å^{-1}, red asterisk $-q$ = 1.04 Å^{-1} and green triangle $-q$ = 0.69 Å^{-1}. Lines are fits of eqn (9) to the data.

presence of the polar ester group in HOT6. HOT6 exhibits two distinct glass transitions, indicated by dielectric α_1- and α_2-relaxations. The α_1-relaxation is assigned to the glassy dynamics of the alkyl side chains in the intercolumnar space while the α_2-relaxation is attributed to the glassy dynamics of the columns. This process can be considered as a glass transition of a one-dimensional liquid. Besides the α-relaxations a γ-relaxation is observed by dielectric spectroscopy. Compared to HAT6 the activation energy of the γ-relaxation is higher for HOT6 which points to a more constrained molecular mobility in the intercolumnar space. This conclusion is supported by a modified low frequency vibrational density of states measured by inelastic neutron scattering.

X-ray diffraction reveals a peak splitting and increased intercolumnar distances in HOT6, indicating altered packing due to conformational variability of the ester groups. Neutron scattering confirms the localized methyl group rotations for HOT6 which are identical to that of HAT6. An additional relaxation process is found by quasielastic neutron scattering. This process shows a close resemblance to the γ-relaxation revealed by dielectric spectroscopy.

Overall, the findings underscore the sensitivity of glassy dynamics to subtle changes in molecular architecture and highlight the importance of combining complementary experimental techniques to unravel the intricate behavior of partially ordered soft matter systems. These insights contribute to the broader understanding of glass transition phenomena in discotic liquid crystals and may inform the design of advanced functional materials for electronic applications.

Author contributions

CK: dielectric spectroscopy and analysis of the dielectric measurement, differential scanning calorimetry, neutron scattering; PS: fast scanning calorimetry, writing; WL and FJ local contacts inelastic and quasielastic neutron time-of-flight scattering; MZ and BF local contacts for neutron backscattering; DAS and FE: X-ray scattering, analysis of the raw X-ray data; RZ: neutron scattering, analysis of raw neutron scattering; AS: data analysis, conception of the project, supervising, writing.

Conflicts of interest

There are no conflicting interests.

Data availability

Supplementary information (SI): examples for raw data of the neutron scattering experiments, section fitting of dielectric data by the HN-function, analysis of dielectric spectra by the derivative approach, estimation of the low frequency density of states, comparison of different analysis methods for elastic scans of HAT6. See DOI: https://doi.org/10.1039/d5sm01247c.

Data will be available from the corresponding author on a reasonable request.

Acknowledgements

The Institut Laue-Langevin (Grenoble/France) and the Heinz Maier-Leibnitz Zentrum (Garching/Germany) are thanked for enabling the neutron scattering experiments. The German Science Foundation is acknowledged for financial support (DFG project numbers 158088440, 282247454 and 430146019).

References

1 P. W. Anderson, Through the Glass Lightly, *Science*, 1995, **267**, 1615–1616.
2 C. A. Angel, Formation of Glasses from Liquids and Biopolymers, *Science*, 1995, **267**, 1924–1935.
3 P. G. Debenedetti and F. H. Stillinger, Supercooled Liquids and the Glass Transition, *Nature*, 2000, **410**, 259–267.
4 J. C. Dyre, Colloquium: The Glass Transition and Elastic Models of Glass-Forming Liquids, *Rev. Mod. Phys.*, 2006, **78**, 953–972.
5 S. Kivelson and G. Tarjus, In Search of a Theory of Supercooled Liquids, *Nat. Mater.*, 2008, **7**, 831–833.
6 J.-H. Hung, T. Patra, V. Meenakshisundaram, J. H. Mangalara and D. S. Simmons, Universal localization transition accompanying glass formation: insights from efficient molecular dynamics simulations of diverse supercooled liquids, *Soft Matter*, 2019, **15**, 9529–9540.
7 V. Lubchenko, Theory of the Structural Glass Transition: A Pedagogical Review, *Adv. Phys.*, 2015, **64**, 283–443.
8 Q. Zheng, Y. Zhang, M. Montazerian, O. Gulbiten, J. C. Mauro, E. D. Zanotto and Y. Z. Mauro, Understanding Glass through Differential Scanning Calorimetry, *Chem. Rev.*, 2019, **119**, 7848–7939.
9 M. Ediger and P. Harrowell, Perspective: Supercooled Liquids and Glasses, *J. Chem. Phys.*, 2012, **137**, 080901–080915.
10 H. Vogel, Das Temperaturabhängigkeitsgesetz der Viskosität von Flüssigkeiten, *Phys. Z.*, 1921, **22**, 645–646.
11 G. S. Fulcher, Analysis of Recent Measurements of the Viscosity of Glasses, *J. Am. Ceram. Soc.*, 1925, **8**, 339–355.
12 G. Tammann and W. Hesse, Die Abhängigkeit der Viscosität von der Temperatur bei unterkühlten Flüssigkeiten, *Z. Anorg. Allg. Chem.*, 1926, **156**, 245–257.
13 C. A. Angell, Relaxation in Liquids, Polymers and Plastic Crystals—Strong/Fragile Patterns and Problems, *J. Non-Cryst. Solids*, 1991, **131–133**, 13–31.
14 C. A. Angell, Entropy and Fragility in Supercooling Liquids, *J. Res. Natl. Inst. Stand. Technol.*, 1997, **102**, 171–185.
15 A. Schönhals, F. Kremer, A. Hofmann, E. W. Fischer and E. Schlosser, Anomalies in the scaling of the dielectric α-relaxation, *Phys. Rev. Lett.*, 1993, **70**, 3459.
16 A. Schönhals, Universal evidence for a crossover behavior of the dynamic glass transition, *Europhys. Lett.*, 2001, **56**, 815.
17 G. Adam and J. H. Gibbs, On the Temperature Dependence of Cooperative Relaxation Properties in Glass-Forming Liquids, *J. Chem. Phys.*, 1965, **43**, 139–146.
18 E. J. Donth, *Relaxation and thermodynamics in polymers: glass transition*, Akademie Verlag, Berlin, 1992.

19 L. Berthier, G. Biroli, J.-P. Bouchaud, L. Cipelletti, D. El Masri, F. Ladieu and M. Pierno, Direct Experimental Evidence of a Growing Length Scale Accompanying the Glass Transition, *Science*, 2005, **310**, 1797–1800.
20 T. Bauer, P. Lunkenheimer and A. Loidl, Cooperativity and the Freezing of Molecular Motion at the Glass Transition, *Phys. Rev. Lett.*, 2013, **111**, 225702-1–225702-5.
21 R. Zallen, *The physics of amorphous solids*, Wiley, New York, 1983.
22 M. Beiner, S. Kahle, S. Abens, E. Hempel, S. Höring, M. Meissner and E. Donth, Low-temperature heat capacity, glass-transition cooperativity, and glass-structure vault breakdown in a series of poly(*n*-alkyl methacrylate)s, *Macromolecules*, 2001, **34**, 5927–5935.
23 X. Monnier, J. Colmenero, M. Wolf and D. Cangialosi, Reaching the ideal glass in polymer spheres: Thermodynamics and vibrational density of states, *Phys. Rev. Lett.*, 2021, **126**, 118004.
24 V. K. Malinovsky, V. N. Novikov and A. P. Sokolov, Investigation of structural correlations in disordered materials by Raman scattering measurements, *J. Non-Cryst. Solids*, 1987, **90**, 485–488.
25 U. Buchenau, Y. M. Galperin, V. L. Gurevich, A. D. Parshin, M. A. Ramos and H. R. Schober, Interaction of soft modes and sound waves in glasses, *Phys. Rev. B: Condens. Matter Mater. Phys.*, 1992, **46**, 2798–2808.
26 B. B. Laird and H. R. Schober, Localized low-frequency vibrational modes in a simple model glass, *Phys. Rev. Lett.*, 1991, **66**, 636–639.
27 S. N. Taraskin, Y. L. Loh, G. Natarajan and S. R. Elliott, Origin of the boson peak in systems with lattice disorder, *Phys. Rev. Lett.*, 2001, **86**, 1255–1258.
28 A. I. Krichikov, A. Jezowski, D. Szewczyk, O. A. Korolyuk, O. O. Romantsova, L. M. Buravtseva, C. Cazoria and J. L. Tamarit, Role of optical phonons and anharmonicity in the appearance of the heat capacity Boson peak-like anomaly in fully ordered molecular crystals, *J. Phys. Chem. Lett.*, 2022, **13**, 5061–5067.
29 W. Schirmacher, G. Diezemann and C. Ganter, Harmonic vibrational excitations in disordered solids and the ''boson peak'', *Phys. Rev. Lett.*, 1998, **81**, 136–139.
30 G. Ding, E. Ma, F. Jiang, S. Cai, N. Xu, B. Cui, L. Dai and M. Jiang, Unified theory of phones in solids with phase diagram of non-Debye anomalies, *Nat. Phys.*, 2025, **21**, 1911–1919.
31 A. Zaccone, A unified picture of phonon anomalies in crystals and lasses, *Sci. China:Phys., Mech. Astron.*, 2026, **69**, 226131.
32 M. Gonzalez-Jimenez, T. Barnard, B. A. Russell, N. V. Tukachev, U. Javonik, L.-A. Hayes, A. J. Farrell, S. Guinane, H. M. Senn, A. J. Smith, M. Wilding, G. Mali, M. Nakano, Y. Miyazaki, P. McMillan, G. C. Sosso and K. Wynne, Understanding the emergence of the boson peak in molecular glasses, *Nat. Commun.*, 2023, **14**, 215.
33 E. Lerner and E. Bouchbinder, Boson-peak vibrational modes in glasses feature hybridized phononic and quasi-localized excitations, *J. Chem. Phys.*, 2023, **158**, 194503.
34 H. Suga and S. Seki, Thermodynamic Studies on Glassy States of Pure Simple Compounds, *J. Non-Cryst. Solids*, 1974, **16**, 171–194.
35 L. M. Wang and R. Richert, Dynamics of glass-forming liquids. IX. Structural versus dielectric relaxation in monohydroxy alcohols, *J. Chem. Phys.*, 2004, **121**, 11170–11176.
36 D. L. Leslie-Pelecky and N. O. Birge, Universal scaling of the relaxation near a model glass transition, *Phys. Rev. Lett.*, 1994, **72**, 1232–1236.
37 B. Kuchta, M. Descamps and F. Affouard, Molecular dynamics study of orientational disorder in cyanoadamantane plastic crystal, *J. Chem. Phys.*, 1998, **109**, 6753–6763.
38 S. Benkhof, T. Blochowicz, A. Kudlik, C. Tschirwitz and E. Rössler, The dielectric response of glass forming propylene carbonate: Slow β-process and excess wing, *Ferroelectrics*, 2000, **236**, 193–207.
39 R. Brand, P. Lunkenheimer and A. Loidl, Relaxation dynamics in plastic crystals, *J. Chem. Phys.*, 2002, **116**, 10386–10401.
40 B. Glüsen, A. Kettner, J. Kopitzke and J. H. Wendorff, On the character of the glass transition in columnar discotics, *J. Non-Cryst. Solids*, 1998, **241**, 113–120.
41 H. Groothues, F. Kremer, P. G. Schouten and J. M. Warman, Charge transport and molecular dynamics in columnar stacks of liquid crystalline phthalocyanine derivatives, *Adv. Mater.*, 1995, **7**, 283–286.
42 C. Krause, H. Yin, C. Cerclier, D. Morineau, A. Wurm, C. Schick, F. Emmerling and A. Schönhals, Molecular dynamics of a discotic liquid crystal investigated by a combination of dielectric relaxation and specific heat spectroscopy, *Soft Matter*, 2012, **8**, 11115–11122.
43 A. Yildirim, A. Bühlmeyer, S. Hayashi, J. C. Haenle, K. Sentker, C. Krause, P. Huber, S. Laschat and A. Schönhals, Multiple Glass Dynamics in Dipole Functionalized Triphenylene Based Discotic Crystals Revealed by Broadband Dielectric Spectroscopy and Advanced Calorimetry – Assessment of the Molecular Origin, *Phys. Chem. Chem. Phys.*, 2019, **21**, 18265–18277.
44 A. Yildirim, C. Krause, R. Zorn, W. Lohstroh, G. J. Schneider, M. Zamponi, O. Holderer, B. Frick and A. Schönhals, Complex molecular dynamics of a symmetric model discotic liquid crystal revealed by broadband dielectric, thermal and neutron spectroscopy, *Soft Matter*, 2020, **16**, 2005–2016.
45 A. Yildirim, M. Kolmangadi, A. Bühlmeyer, P. Huber, S. Laschat and A. Schönhals, Ele ctrical conductivity and multiple glassy dynamics of crown-ether based columnar liquid crystals, *J. Phys. Chem. B*, 2020, **124**, 8728–8739.
46 A. Yildirim, P. Szymoniak, K. Sentker, M. Butschies, A. Bühlmeyer, P. Huber, S. Laschat and A. Schönhals, Dynamics and Ionic Conductivity of Ionic Liquid Crystals Forming a Hexagonal Columnar Mesophase, *Phys. Chem. Chem. Phys.*, 2018, **20**, 5626–5635.
47 M. A. Kolmangadi, A. Yildirim, K. Sentker, M. Butschies, A. Bühlmeyer, P. Huber, S. Laschat and A. Schönhals, Molecular dynamics and electrical conductivity of guanidium based ionic liquid crystals: Influence of cation headgroup configuration, *J. Mol. Liq.*, 2021, **330**, 115666.

48 A. Yildirim, C. Krause, P. Huber and A. Schönhals, Multiple glassy dynamics of a homologous series of triphenylene-based columnar liquid crystals – A study by broadband dielectric spectroscopy and advanced calorimetry, *J. Mol. Liq.*, 2022, **358**, 119212.
49 M. A. Kolmangadi, G. J. Smales, L. ZhuoQing, A. Yildirim, E. Wuckert, S. Eutionnat, F. Demel, P. Huber, S. Laschat and A. Schönhals, Side Chain Length-Dependent Dynamics and Conductivity in Self-Assembled Ion Channels, *J. Phys. Chem. C*, 2022, **126**, 10995–11006.
50 M. A. Kolmangadi, A. R. Raab, P. Szymoniak, Z. Li, P. Huber, S. Laschat and A. Schönhals, Molecular mobility and electrical conductivity of amino acid-based (DOPA) ionic liquid crystals in the bulk state and nanoconfinement, *Phys. Chem. Chem. Phys.*, 2025, **27**, 18162.
51 *Handbook of Liquid Crystals*, ed. D. Demus, J. Goodby, G. W. Gray, H. W. Spiess and V. Vill, Wiley-VCH, Weinheim, 1998.
52 S. Laschat, A. Baro, N. Steinke, F. Giesselmann, C. Hägele, G. Scalia, R. Judele, E. Kapatsina, S. Sauer, A. Schreivogel and M. Tosoni, Discotic Liquid Crystals: From Tailor-Made Synthesis to Plastic Electronics, *Angew. Chem., Int. Ed.*, 2007, **46**, 4832–4887.
53 S. Sergeyev, W. Pisula and Y.-H. Geerts, Discotic liquid crystals: a new generation of organic semiconductors., *Chem. Soc. Rev.*, 2007, **36**, 1902–1929.
54 T. Wöhrle, I. Wurzbach, J. Kirres, A. Kostidou, N. Kapernaum, J. Litterscheidt, J. C. Haenle, P. Staffeld, A. Baro, F. Giesselmann and S. Laschat, Discotic liquid crystals, *Chem. Rev.*, 2016, **116**, 1139–1241.
55 N. Boden, R. J. Bushby, J. Clements, M. V. Jesudason, P. F. Knowles and G. Williams, One-dimensional electronic conductivity in discotic liquid crystals, *Chem. Phys. Lett.*, 1988, **152**, 94–99.
56 V. Mathot, M. Pyda, T. Pijpers, G. Vanden Poel, E. van De Kerkhof, S. van Herwaarden, F. van Herwaarden and A. Leenaers, The Flash DSC 1, a power compensation twin-type, chip-based fast scanning calorimeter (FSC): First findings on polymers, *Thermochim. Acta*, 2011, **522**, 36–45.
57 O. Paris, C. Li, S. Siegel, G. Weseloh, F. Emmerling, H. Riesemeier, A. Erko and P. Fratzl, *J. Appl. Crystallogr.*, 2007, **40**, S466.
58 A. P. Hammersley, FIT2D: a multi-propose data reduction, analysis and visualization program, *J. Appl. Crystallogr.*, 2026, **49**(Part 2), 646–652.
59 F. Kremer and A. Schönhals, Broadband dielectric measurement techniques, in *Broadband Dielectric Spectroscopy*, ed. F. Kremer and A. Schönhals, Springer, 2003, pp. 36–57.
60 M. Bée, Quasielastic neutron scattering, *Principles and applications in solid state chemistry, biology and materials science*, Adam Hilger, 1988.
61 Heinz Maier-Leibnitz Zentrum, TOFTOF: Cold neutron time-of-flight spectrometer, *J. Large-Scale Res. Facil.*, 2015, **1**, A15.
62 F. Rieutord, *INX-Program for time-of-flight data reduction*, ILL internal publication 90RI17T, 1990.
63 B. Frick, The neutron backscattering spectrometer IN16 at the ILL: High energy resolution with high intensity and excellent signal-to-noise ratio, *Neutron News*, 2002, **13**, 15–22.
64 A. Schönhals, B. Frick, C. Krause and R. Zorn, *Elastic Sans on a Homologous Series of Discotic Liquid Crystals*, Institut Laue-Langevin (ILL), 2013, DOI: 10.5291/ILL-DATA.6-05-930.
65 P. Szymoniak, M. A. Kolmangadi, M. Böhning, B. Frick, M. Appel, R. A. Mole, N. R. Souza, R. Zorn and A. Schönhals, Confined Segmental Diffusion in Nanophase Separated Janus-Polynorbornenes as Investigated by Quasielastic Neutron Scattering, *Macromolecules*, 2024, **57**, 8562–8575.
66 K. S. Singwi and A. Sjölander, Diffusive motion in water and cold neutron scattering, *Phys. Rev.*, 1960, **119**, 863.
67 R. Zorn, Neutron scattering studies of dynamics in confined geometries, *Nucl. Instrum. Methods Phys. Res., Sect. A*, 2009, **603**, 439–445.
68 Heinz Maier-Leibnitz Zentrum, SPHERES: Backscattering spectrometer, *J. Large-Scale Res. Facil.*, 2015, **1**, A30.
69 J. Wuttke, A. Budwig, M. Drochner, H. Kämmerling, F.-J. Kayser, H. Kleines, V. Ossovyi, L. C. Pardo, M. Prager, D. Richter, G. J. Schneider, H. Schneider and S. Staringer, SPHERES, Jülich's high-flux neutron backscattering spectrometer at FRM II, *Rev. Sci. Instrum.*, 2012, **83**, 075109.
70 O. G. Randl, SQW – A comprehensive user manual, *ILL internal publication 96RA07T*, 1996.
71 R. Zorn, B. Frick and L. Fetters, Quasielastic neutron scattering study of the methyl group dynamics in polyisoprene, *J. Chem. Phys.*, 2002, **116**, 845–853.
72 A. N. Cammidge and R. J. Bushby, Chapter VII: Synthesis and Structural Features, in *Handbook of Liquid Crystals*, ed., D. Demus, J. Goodby, G. W. Gray, H.-J. Spiess and V. Vill, 1st edn, 1998, vol. 2B, pp. 693–748.
73 https://shop.synthon-chemicals.com/en/LIQUID-CRYSTALS/DISCOTICS/TRIPHENYLENES/2-3-6-7-10-11-Hexakis-heptanoyloxy-triphenylene.html.
74 G. W. Stewart, Theory of X-Ray Diffraction in Liquids, *Phys. Rev.*, 1928, **32**, 558.
75 S. Laschat, A. Baro, N. Steinke, F. Giesselmann, C. Hägele, G. Scalia, R. Judele, E. Kapatsina, S. Sauer, A. Schreivogel and T. Tosoni, Discotic Liquid Crystals: From Tailor-Made Synthesis to Plastic Electronics, *Angew. Chem.*, 2007, **119**, 4916–4950.
76 A. Schönhals and F. Kremer, Analysis of dielectric spectra, in *Broadband Dielectric Spectroscopy*, ed. F. Kremer and A. Schönhals, Springer, Berlin, 2003, pp. 59–98.
77 O. van den Berg, W. G. F. Sengers, W. F. Jager, S. J. Picken and M. Wübbenhorst, Dielectric and Fluorescent Probes to Investigate Glass Transition, Melt, and Crystallization in Polyolefins, *Macromolecules*, 2004, **37**, 2460–2470.
78 M. Wübbenhorst and J. van Turnhout, Analysis of Complex Dielectric Spectra. I. One-Dimensional Derivative Techniques and Three-Dimensional Modelling, *J. Non-Cryst. Solids*, 2002, **305**, 40–49.
79 E. Donth, The Size of Cooperatively Rearranging Regions at the Glass Transition, *J. Non-Cryst. Solids*, 1982, **53**, 325–330.
80 S. W. Lovesey, *Theory of Neutron Scattering from Condensed Matter*, Oxford University, New York, 1987, vol. 1, p. 121.

81 R. Zorn, L. Hartmann, B. Frick, D. Richter and F. Kremer, *J. Non-Cryst. Solids*, 2002, **307**, 547–554.
82 C. Krause, R. Zorn, F. Emmerling, J. Falkenhagen, B. Frick, P. Huber and A. Schönhals, Vibrational density of states of triphenylene based discotic liquid crystals: dependence on the length of the alkyl chain, *Phys. Chem. Chem. Phys.*, 2014, **16**, 7324–7333.
83 W. Schirmacher, B. Schmid, C. Tomaras, G. Viliani, G. Baldi, G. Ruocco and T. Scopigno, *Phys. Status Solidi C*, 2008, **5**, 862–866.
84 M. T. Cicerone and C. L. Soles, Fast Dynamics and Stabilization of Proteins: Binary Glasses of Trehalose and Glycerol, *Biophys. J.*, 2004, **86**, 3836–3845.
85 R. Zorn, H. Yin, W. Lohstroh, W. Harrison, P. M. Budd, B. R. Pauw, M. Böhning and A. Schönhals, Anomalies in the low frequency vibrational density of states for a polymer with intrinsic microporosity – the Boson peak of PIM-1, *Phys. Chem. Chem. Phys.*, 2018, **20**, 1355–1363.
86 R. Zorn, P. Szymoniak, M. Kolmangadi, M. Wolf, D. Alentiev, M. Bermeshev, M. Böhning and A. Schönhals, Low frequency vibrational density of state of highly permeable super glassy polynorbornenes – The Boson peak, *Phys. Chem. Chem. Phys.*, 2020, **22**, 18381–18387.
87 R. Zorn, P. Szymoniak, M. A. Kolmangadi, R. Malpass-Evans, N. B. McKeown, M. Tyagi, M. Böhning and A. Schönhals, Low frequency vibrations and diffusion in disordered polymers bearing an intrinsic microporosity as revealed by neutron scattering, *Crystals*, 2021, **11**, 1482.
88 M. F. T. Telling, Elastic and inelastic fixed window scans, *A practical guide to quasi-elastic neutron scattering*, RSC eTextbook Collection, 2020, ch. 7, 105–119.
89 A. Schönhals, R. Zorn and B. Frick, Inelastic Neutron Spectroscopy as a Tool to Investigate Nanoconfined Polymer Systems, *Polymer*, 2016, **105**, 393–406.
90 J. Colmenero, A. Moreno and A. Alegria, Neutron scattering investigations on methyl group dynamics in polymers, *Prog. Polym. Sci.*, 2005, **30**, 1147–1184.
91 M. Prager and A. Heidemann, Rotational Tunneling and Neutron Spectroscopy: A Compilation, *Chem. Rev.*, 1997, **97**, 2933–2966.